Intensive photochemical oxidation in the marine atmosphere: Evidence from direct radical measurements

Guoxian Zhang[1,2], Renzhi Hu[1, *], Pinhua Xie[1,2,3, **], Changjin Hu[1], Xiaoyan Liu[4], Liujun Zhong[1], Haotian Cai[1], Bo Zhu[5], Shiyong Xia[5],Xiaofeng Huang[5], Xin Li[6], Wenqing Liu[1]

[1] Key Laboratory of Environment Optics and Technology, Anhui Institute of Optics and Fine Mechanics, HFIPS, Chinese Academy of Sciences, Hefei, China

[2] University of Science and Technology of China, Hefei, China

[3] College of Resources and Environment, University of Chinese Academy of Science, Beijing, China

[4] School of Pharmacy, Anhui Medical University, Hefei, China

[5] Key Laboratory for Urban Habitat Environmental Science and Technology, School of Environment and Energy, Peking University Shenzhen Graduate School, Shenzhen, China

[6] State Key Joint Laboratory of Environmental Simulation and Pollution Control, College of Environmental Sciences and Engineering, Peking University, Beijing, China

Correspondence to: Renzhi Hu, Key Laboratory of Environment Optics and Technology, Anhui Institute of Optics and Fine Mechanics, HFIPS, Chinese Academy of Sciences, Hefei, China

****Correspondence to:** Pinhua Xie, University of Science and Technology of China, Hefei, China

Email addresses: rzhu@aiofm.ac.cn (Renzhi Hu); phxie@aiofm.ac.cn (Pinhua Xie)

Abstract: Comprehensive observations of hydroxyl (OH) and hydroperoxy (HO$_2$) radicals were conducted in October 2019 at a coastal continental site in the Pearl River Delta (YMK site, 22.55°N, 114.60°E). The daily maximum OH and HO$_2$ concentrations were (4.7–9.5) $\times$ 10^6 cm^{-3} and (4.2–8.1) $\times$ 10^8 cm^{-3}, respectively. The synchronized air mass transport from the northern cities and the South China Sea exerted a time-varying influence on atmospheric oxidation. Under a typical ocean-atmosphere (OCM), reasonable measurement model agreement was achieved for both OH and HO$_2$ using a 0-D chemical box model incorporating the regional atmospheric chemistry mechanism version 2-Leuven isoprene mechanism (RACM2-LIM1), with daily averages of 4.5 $\times$ 10^6 cm^{-3} and 4.9 $\times$ 10^8 cm^{-3}, respectively. Land mass (LAM) influence promoted more active photochemical processes, with daily averages of 7.1 $\times$ 10^6 cm^{-3} and 5.2 $\times$ 10^8 cm^{-3} for OH and HO$_2$, respectively. Heterogeneous uptake had certain effects on HOx chemistry, but the influence of the halogen mechanism was limited by NOx level. Intensive photochemistry occurred after precursor accumulation, allowing local net ozone production comparable with surrounding suburban environments (5.52 ppb/h during the LAM period). Rapid oxidation process was accompanied by a higher diurnal nitrous acid (HONO) concentration (> 400 ppt). After a sensitivity test, HONO-related chemistry elevated the ozone production rate by 33% and 39% during the LAM and OCM periods, respectively. The nitric acid (P(HNO$_3$)) and sulfuric acid (P(H$_2$SO$_4$)) formation rates also increased simultaneously (~43% and ~48% for LAM and OCM sectors, respectively). In the ozone-prediction test, simulated O$_3$ decreased from ~75 ppb to a global background (~35 ppb) without the HONO constraint, and daytime HONO concentrations were reduced to a low level (~70 ppt). For coastal cities, the particularity of the HONO chemistry tends to influence the ozone-sensitive system and eventually magnifies the background ozone. Therefore, the promotion of oxidation by elevated precursors deserves a lot of attention when aiding pollution mitigation policies.

Keywords: FAGE-LIF; OH and HO$_2$ radicals; Atmospheric oxidation; Marine boundary layer; Precursors;

1 Introduction

The marine boundary layer (MBL) occupies 71% of the planetary boundary layer, is a massive active carbon sink on Earth, and plays an irreplaceable role in coping with global climate change (Stone et al., 2012; Woodward-Massey et al., 2022b; Liu et al., 2022a). As a typical background atmosphere on the Earth, the MBL is equivalent to a natural smog chamber with limited anthropogenic emissions and is characterized by low NOx (the sum of nitric oxide (NO) and nitrogen dioxide (NO_2)) and non-methane hydrocarbons (NMHCs) under a layer of clean air (Woodward-Massey et al., 2022b). The lifetime of OH radical, a key oxidant, is on the order of a few hundred milliseconds (Fuchs et al., 2012). Due to the scarcity of oxidation precursors, including nitrous acid (HONO), formaldehyde (HCHO), and NMHCs, the reaction between O^1D and water vapor generally dominates the radical initiation pathway in the marine environment. For example, in a tropical boundary layer observation experiment (reactive halogens in the marine boundary layer, RHaMBLe), ozone photolysis was found to account for 70% of the OH radical source based on the master chemical mechanism (MCM) (Whalley et al., 2010). The vital role of ozone photolysis is contrasting with typical polluted and semi-polluted areas investigated in a series of field campaigns, in which the propagation routes were found to dominate the radical source (Yang et al., 2021a; Tan et al., 2019a). Therefore, studying the radical chemistry in the MBL provides a valuable opportunity to test the current understanding of atmospheric oxidation mechanisms in a natural setting.

Since the earliest observations off the coast of northern Norfolk in the Weybourne Atmospheric Observatory Summer Experiment in June 1995 (WAOSE95), more observations and simulations of radical chemistry in the MBL environment have been conducted using ground-based, airborne, and shipborne instruments (Qi et al., 2007; Kanaya et al., 2002; Kanaya et al., 2001; Mallik et al., 2018; Woodward-Massey et al., 2022a; Carpenter et al., 2011; Grenfell et al., 1999; Brauers et al., 2001; Whalley et al., 2010). Most field measurements have yielded well-reproduced OH and HO_2 concentration profiles via chemical mechanisms, with differences of within ~20%.

However, the base model is not sufficient to describe the radical chemistry in some exceptional cases, especially in regard to the HO_2 radical. Considering the practical association between halogen (Cl, Br, and I) chemistry and heterogeneous chemistry in marine new particle formation, particularly the involvement of heterogeneous iodine-organic chemistry, exploring the synchronous influence of these mechanisms on HOx (OH and HO_2) radical chemistry in the MBL region is a worthy endeavor (Xu et al., 2022; Huang et al., 2022). The mixing of air masses of continental and marine origins can lead to more variability in radical concentrations. During seasonal measurements of both OH and HO_2 in the Atlantic Ocean, variance analysis indicated that around 70% of the variance of OH and HO_2 was due to diurnal behavior (in the form of photolysis frequency), while the remaining variance was attributed to long-term seasonal cycles (in the form of the changes in O_3, CO and air mass contribution) (Vaughan et al., 2012).

The Chinese economy has undergone rapid development in recent years, and the co-occurrence of primary and secondary regional pollution has become a severe problem (Lu et al., 2019; Liu et al., 2022c). The interactions between air pollutants from upwind cities, shipping vessels, and other anthropogenic emissions lead to precursor accumulation (Sun et al., 2020; Zeren et al., 2022). The background ozone concentration in key regions of China has increased year by year, highlighting the significant influence of anthropogenic activities on the atmospheric oxidation in background regions in China (Wang et al., 2009; Chen et al., 2022). However, little research has been dedicated to the radical chemistry and oxidation mechanism in regions with both coastal and continental features. To fill this research gap, in this study, a field campaign was conducted on photochemistry in the MBL at a coastal site in the Pearl River Delta. The OH and HO_2 radicals associated with other related species were measured in October 2019, and the radical-related oxidation process was identified to determine the photochemical efficiency in the marine atmosphere.

2 Materials and methods

2.1 Site description

As shown in Fig. 1(a), this observation campaign lasted for 11 days from October 18 to October 28, 2019, in Yangmeikeng (YMK, 22.55°N, 114.60°E), a coastal site in Shenzhen, Pearl River Delta. As the core city of the Greater Bay Area, Shenzhen is bordered by Dongguan to the north, Huizhou to the east, and Hong Kong to the south. The YMK site is on the Dapeng Peninsula, to the southeast of Shenzhen, between Mirs Bay and Daya Bay. As it is adjacent to the port of Hong Kong, precursors from ship emissions may influence the atmospheric chemistry. The site is a part of Shenzhen Ecological Monitoring Center station, approximately 35 m above sea level, and the sea is approximately 150 m to the east. No apparent local emissions exist, and the surrounding forest is lush (Fig. 1(b)). Previous literatures reported the monoterpene concentration in the YMK site, with a daily mean of 0.187 ppb (Zhu et al., 2021). Aboundant biogenic emissions will likely influence the local chemistry. In addition to anthropogenic and vegetation emissions, the site is also affected by the synchronization of plumes from northern cities and the South China Sea (Niu et al., 2022; Xia et al., 2021). Due to its significant time-varying pollution characteristics, this area is an ideal site for studying the effects of plume transport on atmospheric oxidation.
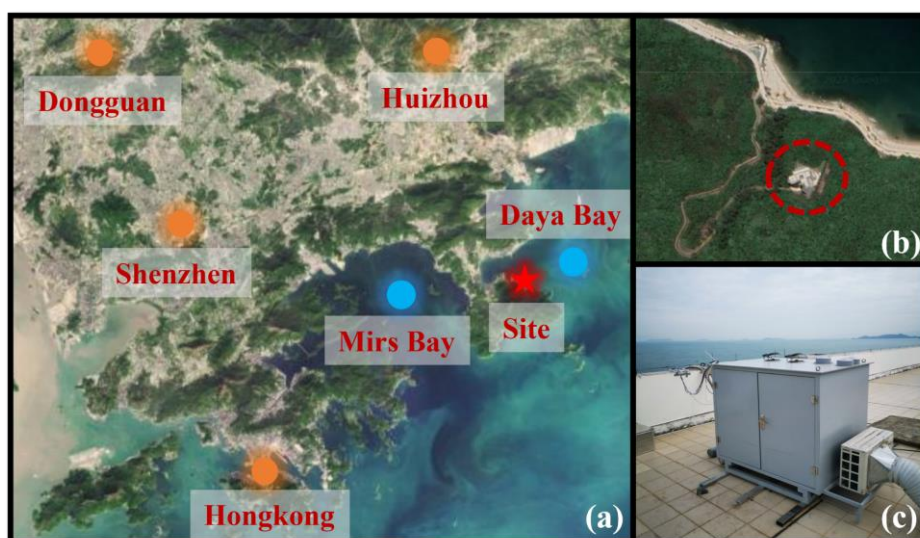
Fig. 1. Details of the observation site**(a)** The location of the measurement site and surrounding cities. The satellite map data is extracted from Google Earth.**(b)** Th close shot of the measurement site location.**(c)** The actual image for the LIF-Box.

Using the hybrid single-particle Lagrangian integrated trajectory (HYSPLIT)

133　model, the 24-h backward trajectories on special days were obtained. In Fig. S1, the

134　red, blue, and green trajectories represent the results at altitudes of 100, 500, and 1000

135　m above ground level, respectively. Two typical transportation pathways dominated

136　the air parcels. One originated from the northern megacities in the Pearl River Delta

137　(defined as the land mass, LAM), especially on October 18, 19, and 27. In contrast, a

138　clean air mass from the east or northeast was mainly transported to the observation

139　site from the ocean (defined as the ocean mass, OCM), with representative episodes

140　on October 22, 25, and 26.

2.2 Instrumentation

2.2.1 HOx radical measurements

143　　The OH and HO_2 radicals were measured via laser-induced fluorescence (LIF).

144　The OH radical can be directly measured by exciting the fluorescence using a 308-nm

145　laser. HO_2 is converted into the OH radical via chemical transformation and then

146　detected in the form of OH radical. The self-developed instrument, the Anhui Institute

147　of Optics Fine Mechanics-LIF (AIOFM-LIF), was used to conduct the measurements

148　(Zhang et al., 2022a; Wang et al., 2021; Wang et al., 2019). This system has been used

149　in key regions of China, including the Yangtze River Delta, Pearl River Delta, and

150　Chengdu-Chongqing region, and achieved good performance in a comparison

151　experiment with a LIF system jointly developed by Forschungszentrum Jülich and

152　Peking University (PKU-LIF) (Zhang et al., 2022b).

153　　The system and detection interference process have been described in detail in

154　previous studies (Zhang et al., 2022a). Briefly, the system consists of a laser output

155　module, a radical detection module, and a control and data acquisition module. These

156　modules are integrated into a sampling box with constant temperature and humidity

157　control (Fig. 1(c)). The laser output module is a union of an Nd:yttrium-aluminum-

158　garnet (YAG) solid-state laser, a 532-nm laser output, and a tunable dye laser. The

159　radical detection module utilized a single pass laser configuration, and the laser beam

160　had a diameter of 8 mm. OH and HO_2 fluorescence cells are combined in parallel and

161　share a common axial optical path. The 308-nm laser is introduced into the HO_2 cell

first and then into the OH cell via an 8-m fiber. To maintain the detection efficiency, the power in the OH fluorescence cell should be at least 15 mW. In the detection process, a set of lenses was deployed and positioned in front of the microchannel plate detector (MCP) to boost the fluorescence collection capacity. Each MCP detector contains a timing control instrument to optimize the signal-to-noise ratio (SNR) of the fluorescence detection. Efficient ambient air sampling was achieved using an aluminum nozzle (0.4 mm orifice), and the pressure in the chamber was maintained at 400 Pa via a vortex vacuum pump (XDS35i, Edwards) to reduce fluorescence quenching.

A wavelength modulation for the background measurement that periodically switches from an on-resonant state to a non-resonant state has been widely used to obtain spectral zero. Since the ozone photolysis interference is due to the laser light itself, wavelength modulation does not allow removing it. Through laboratory experiments, at 20 mW laser energy, every 1% water vapor concentration and 50 ppb ozone concentration can generate a 2.5×10^5 cm^{-3} OH concentration. The results in this paper have subtracted the ozone photolysis interference (Fig. S2). In terms of system design, the AIOFM-LIF system incorporates a short-length inlet design to minimize interferences from ozonolysis and other unknown factors (the distance from radical sampling to flourescence excitation is ~150 mm). An OH measurement comparison with an interference-free instrument, PKU-LIF, was conducted in a real atmosphere in a previous study (Zhang et al., 2022b). The ozonolysis interference on the measurement consistency of both systems was excluded under high-VOCs condition. Overall, the key parameters related to ozonolysis reactions (O_3、alkenes、 isoprene and NOx) in YMK was similar to that during the intercomparison experiment, implies that the chemical conditions do not favor the generation of potential interference to OH measurement (Table S1). For HO_2 measurement, the NO gas (2% in N_2) was utilized to achieve HO_2-to-OH conversion. NO was passed through a ferrous sulfate filter to remove impurities (NO_2, HONO, and so on) before being injected into the detection cell. The NO concentration (~1.6×10^{12} cm^{-3})

7

191 corresponding to a conversion efficiency of ~15% was selected to avoid $RO_2 \rightarrow HO_2$

192 interference (especially from RO_2 radicals derived from long-chain alkanes (C $\geq$ 3),

193 alkenes, and aromatic hydrocarbons). Previous study denoted that the percentage

194 interference from alkene-derived RO_2 under these operating conditions was no more

195 than 5% (Wang et al., 2021).

196   A standard HOx radical source was used to complete the calibration of the

197 detection sensitivity (Wang et al., 2020). The radical source is based on the

198 simultaneous photolysis of H_2O/O_2 by a 185 nm mercury lamp. Humidified air flow is

199 introduced to produce equal amounts of OH and HO_2 radicals after passing the

200 photolysis region. The flow remained in a laminar condition with a maximum flow

201 rate of 20 SLM (standard liters per minute). As the luminous flux in photolysis region

202 is difficult to accurately measure, the linearly correlation between ozone concentration

203 and 185 nm light flux was established. Ozone concentration in the flow tube was

204 measured by a home-made Cavity Ring Down Spectrometer (CRDS, and the

205 detection limit is 15 ppt@30 s, 1σ). Mercury lamp intensity is fine-tuned to establish a

206 correlation between light intensity and ozone concentration. The instrument was

207 calibrated every 1 or 2 days (except for shutdown during rainy periods), and the

208 sensitivity used for the data processing was an average of all of the calibration results.

209 In the YMK campaign, the relative humidity varied between 40 – 80% (Fig. S3). In

210 order to test different atmospheric conditions, both low (~40%) and high (~70%)

211 levels of water vapor were selected to produce OH and HO_2 radicals for calibration,

212 and the corresponding HOx concentration obtained from the standard source was 1.0

213 $\times 10^9$ cm^{-3} and 1.8×10^9 cm^{-3}, respectively (Zhang et al., 2022b).

214   Considering the system uncertainty and calibration uncertainty, the detection

215 limits of the OH and HO_2 radicals were 3.3×10^5 cm^{-3} and 1.1×10^6 cm^{-3} (60 s, 1σ),

216 respectively. At a typical laser power of 15 mW, the measurement accuracy for OH

217 and HO_2 measurement was 13% and 17% (1σ), respectively.

218 **2.2.2 Supporting measurements**

219   In addition to measuring the HOx radicals, an extensive suite of relevant species

220　was also measured close to the LIF instrument to improve the analysis of the radical

221　photochemistry. Detailed information about the measurement instrument is presented

222　in Table S2, including the meteorological parameters (wind speed (WS), wind

223　direction (WD), temperature (T), relative humidity (RH), pressure (P), and solar

224　radiation (J-values)) and chemical parameters (ozone (O_3), carbon monoxide (CO),

225　sulfur dioxide (SO_2), HONO, NO, NO_2, HCHO, NMHCs, and particulate matter

226　($PM_{2.5}$)). HONO measurement was conducted using a commercial Long-Path

227　Absorption Photometer (LOPAP). The LOPAP method utilizes two absorption tubes

228　in series for differential correction, which effectively eliminates the influence of

229　known interfering substances such as NO_2 and N_2O_5, offering an advantage over

230　traditional wet chemistry methods. Zero air measurements were taken every 8 hours

231　for a duration of 20 minutes to correct for instrument baseline fluctuations. This

232　method has been extensively tested for its suitability in detecting HONO in complex

233　atmospheric conditions, as demonstrated in previous studies by (Yang et al., 2022a;

234　Yang et al., 2021b; Wang et al., 2023). Eight measured photolysis rates (j(NO_2),

235　j(H_2O_2), j(HCHO), j(HONO), j(NO_2), j(NO_3), j(O1D)) were used as model constraints.

236　In addition to HCHO, other volatile organic compounds (VOCs) were detected using

237　a gas chromatograph coupled with a flame ionization detector and mass spectrometer

238　(GC-FID-MS). Ninety-nine types of VOCs, including C_2–C_{11} alkanes, C_2–C_6 alkenes,

239　C_6–C_{10} aromatics, halohydrocarbons, and some oxygenated VOCs (OVOCs), were

240　observed using the GC-FID-MS at a 1-h time interval. Only isoprene was considered

241　as a representative of biogenic VOCs (BVOCs). All of the instruments were located

242　close to the roof of the monitoring building, nearly 12 m above the ground to ensure

243　that all of the pollutants were located in a homogeneous air mass.

244　2.3 Model description

245　　A 0-D chemical box model incorporating a condensed mechanism, the regional

246　atmospheric chemistry mechanism version 2-Leuven isoprene mechanism (RACM2-

247　LIM1), was used to simulate the radical concentrations and the generation of ozone

248　(Stockwell et al., 1997; Griffith et al., 2013; Tan et al., 2017). The meteorological

parameters, pollutants, and precursor concentrations mentioned in Section 2.2.2 were input into the model as boundary conditions. All of the constraints were unified to a temporal resolution of 15 min through averaging or linear interpolation. The overall average during the observations was substituted for large areas of missing data due to instrument maintenance or failure. Three days of data were entered in advance as the spin-up period, and a synchronized time-dependent dataset was eventually generated. The hydrogen (H_2) and methane (CH_4) concentrations were set to fixed values of 550 ppb and 1900 ppb, respectively. The physical losses of species due to processes such as deposition, convection, and advection were approximately replaced by an 18 h atmospheric lifetime, corresponding to first order loss rate of ~1.5 cm/s (by assuming a boundary layer height of about 1 km). The sensitivity analysis shows that when the lifetime changes within 8 – 24 hours, the values differed less than 5% for both OH, HO_2, k_{OH} (Fig. S4). According to the measurement accuracy, the simulation accuracy of the model for the OH and HO_2 radicals was 50% (Zhang et al., 2022a).

In addition, another steady-state calculation method (PSS) can also be used to estimate the concentrations of OH and HO_2 radicals (Eq. (1)(2), (Woodward-Massey et al., 2022b; Slater et al., 2020)). Since the k_{OH} and RO_2 concentrations were not obtained in this observation, simulated values are used as substitutes. Other radical and reactive intermediates are actual values that measured from the instruments in Table S2.

$$[OH]_{PSS} = \frac{j_{HONO}[HONO] + \varphi_{OH}j(O^1D)[O_3] + k_{HO_2+NO}[NO][HO_2]}{k_{OH}} \quad (1)$$

$$[HO_2]_{PSS} = \frac{k_{CO+OH}[CO][OH] + j_{HCHO}[HCHO] + k_{RO_2+NO}[NO][RO_2]}{k_{HO_2+NO}[NO]} \quad (2)$$

Considering the environmental characteristics of the MBL, the gas-phase mechanisms for bromine (Br) and iodine (I) were introduced into the base model to diagnose the impacts of the reactive bromine and iodine chemistry. The details of the mechanisms involved are listed in Tables S3 and S4. The halogen species were not available in the YMK site, so the typical levels of BrO and IO concentration in MBL site was used as a reference value (average daytime concentration of ~5 ppt) (Xia et al., 2022; Bloss et al., 2010; Whalley et al., 2010).

278   The heterogeneous uptake of HO_2 is considered to play an important role in the

279   MBL region (Whalley et al., 2010; Zou et al., 2022; Woodward-Massey et al., 2022b).

280   In order to assess the impact of HO_2 uptake on HOx radical chemistry, we

281   incorporated HO_2 uptake reaction into the base model (Eq. (3) - (5)).

282    $$HO_2 + uptake \rightarrow products \tag{3}$$
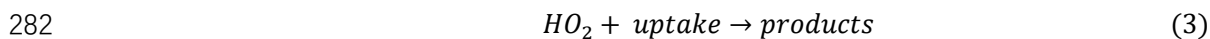
283    $$k_{HO_2+uptake} = \frac{\gamma \times ASA \times \nu_{HO_2}}{4} \tag{4}$$

284    $$\nu_{HO_2} = \sqrt{\frac{8 \times R \times T}{0.033 \times \Pi}} \tag{5}$$

285   Here, ASA represents the aerosol surface area [μm^2 cm^{-3}], which can be estimated

286   as 20 times the $PM_{2.5}$ concentration [$\mu g/cm^3$]. ν_{HO_2} [cm^{-1}] can be calculated using Eq.

287   (5), where T and R represent the temperature and gas constant, respectively. The

288   heterogeneous uptake coefficien (γ) for HO_2 usually has high uncertainty, with typical

289   values ranging from 0 to 1 (Song et al., 2021). In this study, we set γ to 0.08 to

290   evaluate the influence of HO_2 uptake on radical concentrations.

3 Results

3.1 Meteorological and chemical parameters

293   Fig. S3 presents the time series of the main meteorological parameters and

294   pollutants during the observation period at the YMK site. Except for on 2 days,

295   October 26 and 28, the meteorological characteristics of the other days were generally

296   stable. The daily maximum T, RH, and J-values did not vary significantly. The

297   suitable temperature (20–30°C) and humidity (40–80%) conditions promoted the

298   stable oxidation of the diurnal photochemistry. The peak $j(O^1D)$ value was

299   approximately 2.0×10^{-5} s^{-1}, exhibiting the typical characteristics of intense light

300   radiation in autumn in the Pearl River Delta region (Yang et al., 2022a; Tan et al.,

301   2022).

302   As typical marine air components, the concentrations of NOx, CO, $PM_{2.5}$, and

303   other pollutants were lower than those detected in other observation campaigns in

304   both urban and suburban areas in the Pearl River Delta region (Tan et al., 2019b; Lu et

al., 2012; Yang et al., 2022b). Serval observation campaigns have discovered the relationship between wind direction and radical chemistry (Lu et al., 2012; Fuchs et al., 2017; Niu et al., 2022). Although there was no apparent wind speed condition, the dominant air mass still influenced the pollutant concentrations due to the particularity of the marine site.
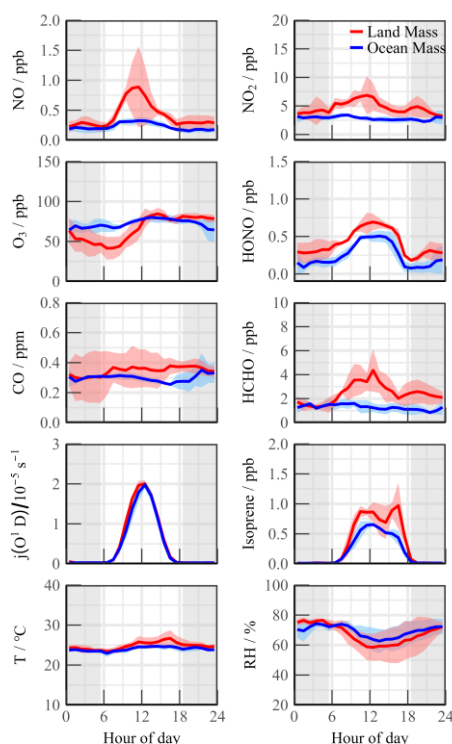
Fig. 2. Mean diurnal profiles of measured trace gases parameters during Land mass and Ocean mass episodes. The coloured shadows denote the 25 and 75% percentiles. The grey areas denote nighttime.

During the OCM period, the NOx and HCHO concentrations exhibited relatively clean characteristics that were consistent with those previously observations in open ocean (RHaMBLe, SOS, CHABLIS and ALBATROSS, Table 1). Isoprene, a representative BVOC, achieved a diurnal concentration of 0.58 ± 0.06 ppb, indicated slightly local emissions could have impacted the concentrations of the precursor species even in OCM sector. The ozone concentration in the YMK site was always at the critical value of the updated Class I standard (GB3095-2012, average hourly O_3 of 81 ppb at 25°C and 1013 kPa). The occurrence of fewer emissions reduced the titration effect, resulting in the ozone exhibiting no apparent diurnal trend on some of the dates and a high background value at night (78.1 ± 7.6 ppb).

As a coastal site, chemical conditions could be influenced by local land emissions

depending on the wind direction. Compared with the OCM period, the meteorological

conditions (T, RH, and J-values) changed slightly during the LAM episode, but the

pollutants were accumulated due to the transport of the plume from the northern cities

(Fig. 2). The CO and PM$_{2.5}$ concentrations exhibited good consistency and even mild

pollution features ((0.36 ± 0.12 ppm) and (37.70 ± 7.91 µg/m^3), respectively),

reflecting the influence of human activities. Both NO and NO$_2$ peaked at around

10:00, exhibiting prominent pollution characteristics. HONO exhibited a distribution

with high daytime (0.66 ± 0.08 ppb) and low nighttime (0.33 ± 0.09 ppb)

concentrations. This unique distribution of HONO has been observed in remote

environments in several previous observation campaigns (Jiang et al., 2022; Crilley et

al., 2021). High HONO concentration in the daytime will affect the chemical

composition of the atmosphere and the secondary pollution generation.

Table 1. Summary of radical concentrations and related species concentrations at MBL. All data are listed as the average in noontime (10:00~15:00).

Campaign	Location	Category	Date	OH (10^{6}cm^{-3})	HO$_2$ (10^{8}cm^{-3})	HCHO (ppb)	HONO (ppb)	NOx (ppb)	O$_3$ (ppb)	Reference
WAOSE95	Weybourne, UK	Coastal	1995 (Jun)	5.0	-	1.50	0.10	<2.0	40.0	(Grenfell et al., 1999)
ALBATROSS	Atlantic Ocean	Open ocean	1996 (Oct-Nov)	7.0	-	0.50	-	-	25.0	(Brauers et al., 2001)
EASE96	Mace Head, Ireland	Coastal	1996 (Jul-Aug)	2.3	2.6	-	-	~1.0	45.0	(Carslaw et al., 1999)
EASE97	Mace Head, Ireland	Coastal	1997 (Apr-May)	1.8	1.0	0.70	-	0.95	46.0	(Creasey et al., 2002)
ORION99	Okinawa Island, Japan	Coastal	1999 (Aug)	4.0	4.3	-	0.20	6.3	23.0	(Kanaya et al., 2001)
RISOTTO	Rishiri Island, Japan	Coastal	2000 (June)	7.4	3.1	-	-	0.45	-	(Kanaya et al., 2002)
RISFEX	Rishiri Island, Japan	Coastal	2003 (Aug)	2.7	1.5	-	-	0.2	28.0	(Qi et al., 2007)
CHABLIS	Antarctica	Open ocean	2005 (Jan-Feb)	1.0	1.1	0.12	0.007	0.02	7.0	(Bloss et al., 2010)
RHaMBLe	Atlantic Ocean	Open ocean	2007 (May-Jun)	9.0	6.0	0.30	-	0.014	35.0	(Whalley et al., 2010)
SOS	Cape Verde, Atlantic Ocean	Open ocean	2009 (Jun; Sep)	9.0	4.0	1.9	-	0.050	40.0	(Carpenter et al., 2011)
CYPHEX	Cyprus, Mediterranean	Coastal	2014 (Jul)	5.8	6.3	~1.0	~0.080	<1.0	69.0	(Mallik et al., 2018)
ICOZA (NW-SE)	North Norfolk, UK	Coastal	2015 (Jul)	3.0	1.4	0.9	0.052	2.0	39.0	(Woodward-Massey et al., 2022b)
ICOZA (SW)	North Norfolk, UK	Coastal	2015 (Jul)	4.1	1.0	1.1	0.097	3.0	31.0	(Woodward-Massey et al., 2022b)
HT	Hok Tsui, China	Coastal	2020 (Oct-Nov)	4.9	-	1.0	0.15	~4.0	65.0	(Zou et al., 2022)

13

| YMK (Land Mass) | Shenzhen, China | Coastal | 2019 (Oct) | 7.1 | 5.2 | 3.4 | 0.66 | 6.4 | 75.6 | This work |
| YMK (Ocean Mass) | Shenzhen, China | Coastal | 2019 (Oct) | 4.5 | 4.9 | 1.2 | 0.48 | 3.0 | 78.1 | This work |

The detailed information for VOCs species during the YMK campaign has been added in the Table S5. The daily maximum NMHC concentration peaked at 27.81 ± 9.91 ppb, and the maximum value of ~40 ppb occurred on October 27. Local biological emissions significantly affected the NMHC composition of the site, and isoprene achieved a noon maximum of 0.82 ± 0.16 ppb. Neither anthropogenic alkenes (2.21 ± 0.94 ppb) nor aromatic (1.31 ± 0.25 ppb) hydrocarbons were abundant, and OVOCs accounted for approximately 50% of the total. As a photochemical indicator, formaldehyde peaked at ~4 to ~8 ppb during the LAM episode, suggesting a more vigorous oxidation process. The HONO concentration was 6.8 times higher than the SW scenario in the ICOZA observation (a pollution period dominated by a southwest wind direction), while the HCHO concentration was 3.1 times higher. (Woodward-Massey et al., 2022b). The abundance of oxidation precursors (HONO, HCHO, O_3, and NMHCs) reflected the unique atmospheric conditions in the marine environment in China, which originated from the complex atmospheric pollution.

3.2 HOx radical concentrations and modelled OH reactivity

Fig. 3(a)(b) shows the time series of the simulated and observed OH and HO_2 radical concentrations during the observation campaign. The time series of the simulated OH reactivity (k_{OH}) is presented in Fig. 3(c). The observed OH and HO_2 radicals exhibited significant diurnal trends. The daily maximum OH and HO_2 values were $(4.7–9.5) \times 10^6 \, \text{cm}^{-3}$ and $(4.2–8.1) \times 10^8 \, \text{cm}^{-3}$, respectively. The peak k_{OH} value was commonly less than 10 s^{-1}. Due to human activities, the simulated k_{OH} reached more than ~15 s^{-1} on some days. The radical concentrations and reactivity exhibited similar trends, which differed from reports on urban and semi-urban areas where inorganic species (NOx and CO) were the dominant controllers of k_{OH} (Zhang et al., 2022a; Tan et al., 2019b; Lou et al., 2010). The k_{OVOCs} was separated into $k_{OVOCs(Obs)}$ and $k_{OVOCs(Model)}$ (Fig. 3(c)). Specifically, $k_{OVOCs(Obs)}$ includes the observed species

such as formaldehyde (HCHO), acetaldehyde (ACD), higher aldehydes (ALD), acetone (ACT), ketones (KET), and oxidation products of isoprene (MACR and MVK). The model-generated intermediates, such as glyoxal, methylglyoxal, methylethyl ketone, and methanol, are categorized as $k_{OVOCs(Model)}$. Approximately 50% of the total k_{OVOCs} are represented by unconstrained species ($k_{OVOCs(Model)}$), which contribute a daily k_{OH} of 1.39 s^{-1}. Overall, the observed OH and HO$_2$ concentrations were both well reproduced by the base model incorporating the RACM2-LIM1 mechanism. The observed OH was underestimated only on the first days, and a slight model overestimation happened on October 23&24. PSS calculation showed good agreement with the base model, providing evidence of the balance of radical internal consistency in the daytime. It should be noted that the OH reactivity of unmeasured VOCs may be underestimated due to the lumped groups in RACM2 mechanism.
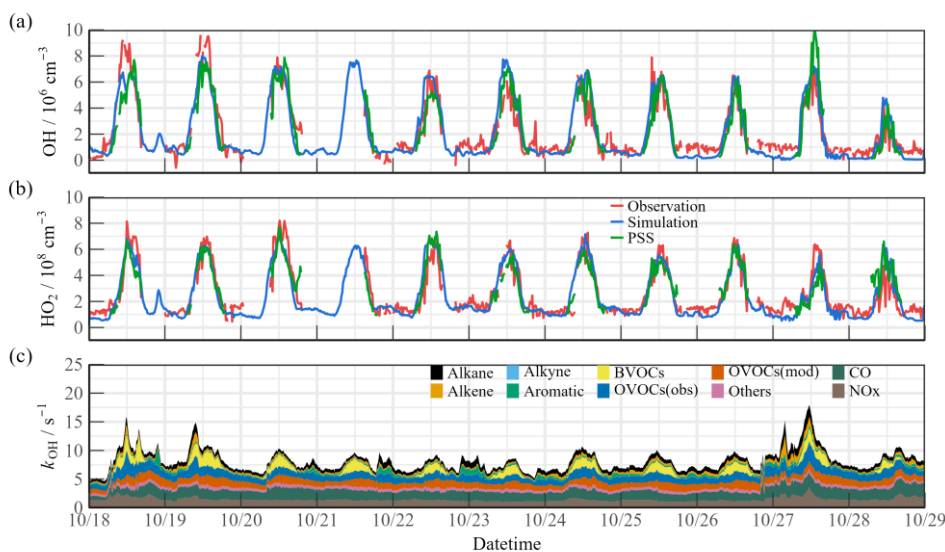
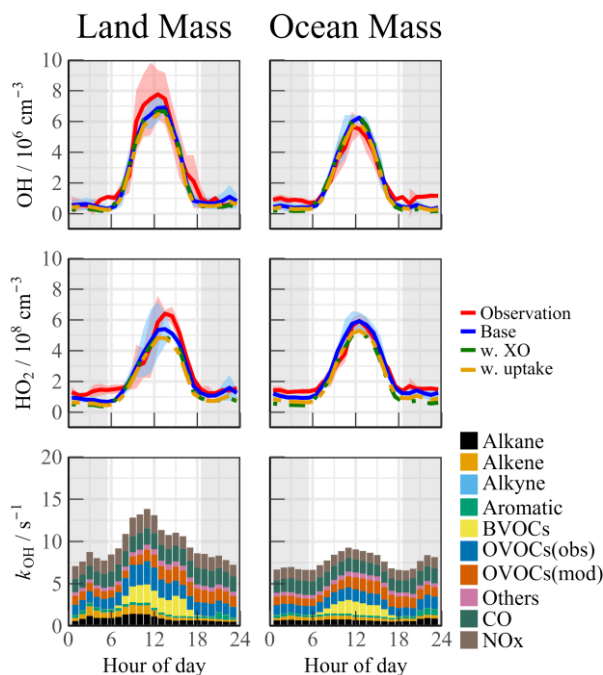**Fig. 3.** Timeseries of the observed and modelled parameters for OH, HO$_2$ and k_{OH} during the observation period. **(a)** OH, **(b)** HO$_2$, **(c)** k_{OH}.

The air mass transport of the precursors induced photochemistry accumulation, which was then reflected in the changes in the oxidation progress. It is worth comparing the concentrations and reactivities of the radicals by classifying the predominant air mass (Fig. 4). During the OCM period, the observed OH and HO$_2$ radicals could be reflected by the base chemical mechanism, with daily averages of 4.5×10^6 cm^{-3} and 4.9×10^8 cm^{-3}, respectively. Compared to other campaigns (Table 1), the observed maximum values were within reasonable ranges (OH: $2 - 9 \times 10^6$

15

387 cm^{-3}; HO$_2$: $1 - 6 \times 10^8$ cm^{-3}). Despite low NOx levels during the OCM period, the

388 HO$_2$ radical was not overestimated using the base model, which was dissimilar to

389 many MBL observations (Bloss et al., 2010). However, both the OH and HO$_2$ radical

390 concentrations reached higher levels during the LAM-dominant period, indicating a

391 more active photochemical process (Section 4.1). The diel averages for the OH and

392 HO$_2$ radicals were 7.1×10^6 cm^{-3} and 5.2×10^8 cm^{-3}, respectively, which were

393 notably higher than the levels reported in the ICOZA observations (Woodward-

394 Massey et al., 2022b). The base scenario underestimated both the OH and HO$_2$

395 concentrations between 10:00 and 15:00, and the observation-to-model ratio was

396 greater than 1.2. The calculated daily maximum total OH reactivity was 8.8 s^{-1}, and

397 nearly 70% of the reactivity was accounted for by the organic species, among which

398 the OVOCs were the largest contributor (30.6%). The anthropogenic alkanes, alkenes,

399 and aromatic hydrocarbons contributed less than 10% to the reactivity. Compared

400 with the OCM-dominant episode, the higher reactivity during the LAM period

401 indicated the occurrence of efficient recycling during the ROx (the sum of OH, HO$_2$,

402 and RO$_2$) propagation (12.4 s^{-1} vs. 8.8 s^{-1}). The higher contributions of the BVOCs

403 (only isoprene was considered, 15.6%) and OVOCs (30.2%) to the reactivity reflected

404 the diverse composition of the VOCs in the forest environment. Under enhanced

405 photochemistry, the calculated OH reactivity could be an underestimation of the total

406 OH reactivity, so a missing OH source may be masked. As a representative of the

407 OVOCs, HCHO reflects the photochemical level to a certain extent. As shown in Fig.

408 S5, a solid positive dependence between the OH$_{obs}$-to-OH$_{mod}$ ratio and HCHO was

409 observed (the daytime data were restricted according to j(O^{1}D) $> 5 \times 10^{-6}$ s^{-1}). With

410 the increase of photochemical intensity, the ratio between the observed and simulated

411 OH radical showed an obvious mismatch. Obtaining the full magnitude of the radical-

412 related parameters is necessary to compensate for the discrepancy in the concentration

413 closure experiments.

Fig. 4. Median diurnal profiles of the observed and modelled OH, HO₂, k_{OH} during LAM and OCM episodes. The coloured shadows for OH and HO₂ radicals denote the 25 and 75% percentiles. The grey areas denote nighttime.

Halogen species have been recognized as potent oxidizers that can boost photochemistry (Xia et al., 2022; Peng et al., 2021). A sensitivity test was performed by imposing BrO and IO into the base model to diagnose the impact of the halogen chemistry on the troposphere chemistry. The concentration of BrO and IO is set to ~5 ppt, which is a typical level in MBL site (Xia et al., 2022; Bloss et al., 2010; Whalley et al., 2010). The details of the mechanisms involved are listed in Tables S3 and S4. In this scenario (Fig. 4, green line). The daytime concentration of HO₂ radical decreased by 8.5% and 13.3% during the LAM and OCM periods, respectively, compared to the base model. However, there was no significant change in the concentration of OH radicals (<3%). Traditionally, it is believed that the inclusion of halogen chemistry leads to higher modelled OH concentrations and lower modelled HO₂ concentrations. Therefore, the lack of an increase in OH concentration with the introduction of the halogen mechanism at the YMK site calls for further investigation (Fig. S6). By modifying the NO concentration in different levels (Scenario 1: [NO] × 150%, Scenario 2: base, Scenario 3: [NO]×20%, Scenario 4: [NO]×10%), the response of HOx radicals to the halogen mechanism varied under different NO levels. As the

17

constrained NO increased from 30 ppt to 500 ppt, the reduction in HO$_2$ radicals due to the Br and I mechanisms ranged between 10% and 20%. At elevated NOx levels, reactions between halogen radicals and NOx occurred, inhibiting the formation of OH radicals. In Scenario 1, the OH concentration even decreased by 3.5% when introducing the halogen mechanism. When NO concentration was constrained around 30 ppt (Scenario 4), similar to those obtained in RHaMBLe/CYPHEX campaigns, the modelled OH concentration increased by 14.4%, while the HO$_2$ concentration decreased by approximately 20.8% (Whalley et al., 2010; Bloss et al., 2010). Therefore, the sensitivity of OH radicals to the halogen mechanism in the YMK region is primarily limited by the local NOx concentration level.

Alough the modelled and measured HO$_2$ showed good agreement，the effect of HO$_2$ heterogeneous processes on the chemistry of HOx radicals is also worth exploring. The inclusion of heterogeneous processes ($\gamma = 0.08$) did reduce the modelled HO$_2$ concentration for ~10% during both LAM and OCM periods (Fig. 4, yellow line). This reduced agreement between observation and simulation emphasizes the presence of a missing HO$_2$ source in the base model.

4 Discussion

4.1 Experimental radical budget balance

4.1.1 OH radical

A process-oriented experiment was conducted to investigate the photochemistry progress from a budget balance perspective (Woodward-Massey et al., 2022a; Tan et al., 2019b; Yang et al., 2021a). The OH was in a photostationary steady state due to its short lifetime. The total OH removal rate was directly quantified from the union of the OH concentration and the reactivity (Eq.(6)):

$$D(OH) = [OH] \times k_{OH}. \tag{6}$$

The total production rate of the OH radical was the sum of the primary sources (O$_3$/HONO photolysis and ozonolysis reactions) and secondary sources (HO$_2$ + NO) (Eq.(7)):

$$462 \qquad P(OH) = j_{HONO}[HONO] + \varphi_{OH}j(O^1D)[O_3] + \Sigma i \left\{ \varphi_{OH}^i k_{Alkenes+O_3}^i [Alkenes][O_3] \right\}$$

$$463 \qquad + (k_{HO_2+NO}[NO] + k_{HO_2+O_3}[O_3])[HO_2] . \qquad (7)$$

464 Here, φ_{OH} and φ_{OH}^i represent the OH yields in the O_3 photolysis and alkene

465 ozonolysis processes, respectively.

466 The diel profiles of the experimental OH budget during the LAM and OCM

467 periods are shown in Fig. 5. Both the observed OH and HO_2 radicals were introduced

468 into the budget calculations. Because k_{OH} was not measured during the observation

469 experiment, the simulated value was used to analyze the removal rate. Therefore,

470 D(OH) should be considered a lower limit as it uses calculated rather than measured

471 k_{OH} (Yang et al., 2022b). During the OCM period, the HO_2 + NO reaction accounted

472 for ~50% of the OH yield. The maximum of 6.6 ppb/h occurred at around 12:00. The

473 photolysis reactions could increase the daytime contributions of HONO and O_3 to

474 1.52 ppb/h and 0.84 ppb/h, respectively (10:00–15:00). The contribution of the non-

475 photolytic radical source (ozonolysis reactions) was almost negligible.
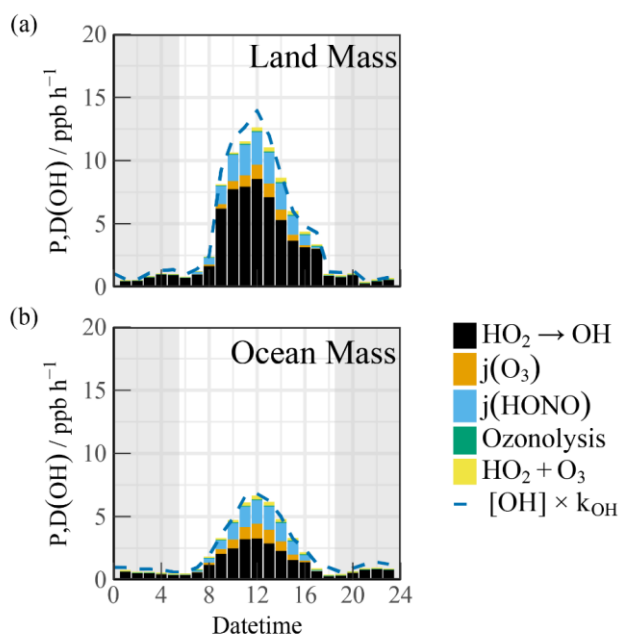
476
477 **Fig. 5.** The diurnal profiles of the experimental OH budget during **(a)** LAM and **(b)** OCM episodes. The blue
478 line denotes the OH destruction rate([OH]×k_{OH}). The grey areas denote nighttime.

479 Compared with other marine observations, the calculated OH generation rate was

480 approximately twice that reported in the ICOZA and five times that obtained in the

481 RHaMBLe campaigns (Woodward-Massey et al., 2022a; Whalley et al., 2010).

During the LAM period, the OH generation rate reached a maximum of 12.6 ppb/h, accompanied by a secondary source contribution of 67% (from the reaction between HO_2 and NO) during the daytime, which was close to several observations related to polluted plumes (Woodward-Massey et al., 2022a; Tan et al., 2019b; Lu et al., 2012; Yang et al., 2022b). When the simulated k_{OH} was introduced into the experimental budgets, the difference between P(OH) and D(OH) was less than 2 ppb/h.

4.1.2 Total ROx radicals

The budget analysis of the HO_2 and RO_2 radicals could not be performed well due to the lack of RO_2 radical observation data. The diurnal profiles of the ROx production (P(ROx)) and termination rate (L(ROx)) for the different air masses are shown in Fig. 6. The P(ROx) could reach 3.36 ppb /h with an ocean plume. HONO photolysis controlled nearly half of the primary sources (45.7%), and the daily distribution was consistent with that of solar radiation. The ozone-related contributions from photolysis and ozonolysis were approximately 46.6% (25.1% from photolysis and 11.5% from ozonolysis,respectively). The remaining contribution was from the photolysis of carbonyls (HCHO and OVOCs) (15.0%). The anthropogenic contribution to the radical chemistry was not ignorable, and the ROx source in this observation was exponentially higher than that in other MBL observations (Woodward-Massey et al., 2022a; Stone et al., 2012; Whalley et al., 2010; Mallik et al., 2018). The P(ROx) of the LAM was close to that in Shenzhen (~4 ppb/h) but was significantly lower than that in Yufa (~7 ppb/h) and the BackGarden (~11 ppb/h) (Tan et al., 2019b; Lu et al., 2012; Yang et al., 2022b). The reactions between ROx and NOx and self-combination were the main pathways of radical termination (~70%). The contribution of the formation of peroxynitrate to the L(ROx) could not be ignored in the daytime.
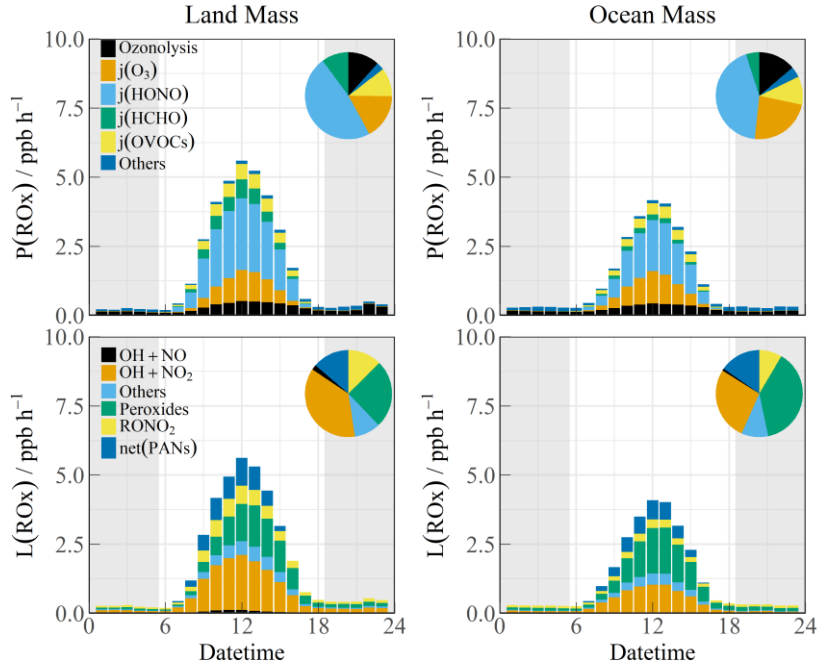
Fig. 6. The diurnal profiles of ROx budget during Land mass and Ocean mass episodes. The pie chart denotes proportions in different parts during the daytime (10:00-15:00). The grey areas denote nighttime.

The high daytime HONO concentrations observed at the YMK site is a notable phenomenon. Due to the high HONO concentration during the daytime, the photolysis reaction made daytime contributions of 1.52 ppb/h and 2.19 ppb/h during the OCM and LAM periods, respectively. As the only known gas-phase source, OH + NO accounted for a negligible proportion of the HONO production rate. Given the location of the site, HONO from cruise ship emissions is a possible component of the primary anthropogenic source (Sun et al., 2020). Other active tropospheric HONO sources (heterogeneous reactions with NO_2 and $p(NO_3^-)$ photolysis) are worthy of consideration and significantly contribute to the atmospheric oxidation in the MBL area (Zhu et al., 2022; Crilley et al., 2021).

4.2 Local ozone production rate

Peroxy radical chemistry is the essential photochemical source of tropospheric ozone (F(Ox), Eq.(8)):

$$F(O_x) = k_{HO_2+NO}[NO][HO_2] + \sum_i (1-\alpha_i) k_{RO_2^i+NO}[NO]RO_2^i \qquad (8)$$

NO reacts with HO_2 and RO_2 radicals to form NO_2, and then, photolysis occurs to form O_3 under solar radiation. NO_2 and ozone are the two sides of the oxidation reservoir. The effect of local emissions on the photodynamic equilibrium can be avoided by characterizing the photochemical production of the total oxidants (Tan et

21

528　al., 2019b). α_i represents the organic nitrate yield, which affects the amount of NO_2

529　that is produced from the reaction between RO_2 and NO (Tan et al., 2018b). Ox is

530　mainly photochemically removed through ozone photolysis, ozonolysis, radical chain

531　propagation ($OH/HO_2 + O_3$), and chain termination ($OH + NO_2$) reactions in the

532　troposphere (D(Ox), Eq.(9)):

$$D(O_x) = \varphi_{OH} j(O^1 D)[O_3] + \Sigma i \left\{ k^i_{Alkenes+O_3}[Alkenes][O_3] \right\} + (k_{O_3+OH}[OH] +$$

533

$$k_{O_3+HO_2}[HO_2])[O_3] + k_{OH+NO_2}[OH][NO_2] \qquad (9)$$

534

535　The net formation rate $P(O_x)$ can be calculated by subtracting D(Ox) from F(Ox)

536　(Eq.(10)):

$$P(O_x) = F(O_x) - D(O_x) \qquad (10)$$

537

538　　The simulated RO_2 radical concentration was introduced into the F(Ox)

539　calculation. The diurnal variations in the ozone generation in the different air masses

540　are shown in Fig. 7. The contribution of the HO_2 radical to F(Ox) was approximately

541　60%. The RO_2 radicals consisted of various types such as methyl peroxy (MO_2),

542　acetyl peroxy radicals (ACO_3/RCO_3), and other radicals derived from alkanes

543　(ALKAP), alkenes (ALKEP), and isoprene (ISOP), which accounted for an additional

544　40% of the F(Ox). On a daytime basis, the maximum F(Ox) reached 7.4 ppb/h at

545　around 12:00 in the OCM period, while a persistent-high value (maximum of 12.5

546　ppb/h at 10:00–14:00) occurred in the LAM period. A vast amount of Ox was

547　consumed in the nitric acid ($OH + NO_2$) formation pathways, i.e., higher than the

548　ozonolysis removal. The daily averaged ozone production rates were 5.52 and 2.76

549　ppb/h during the LAM and OCM periods, respectively.
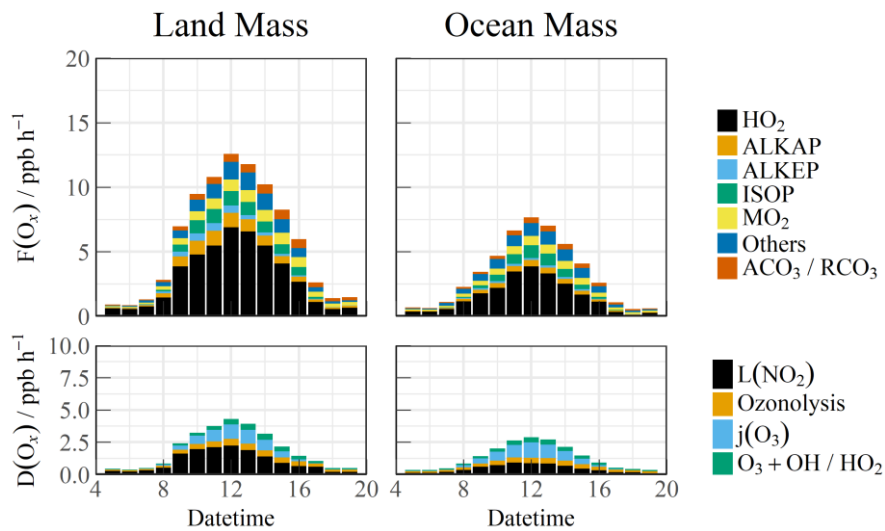
550

4.3 Relationship between precursors and oxidation rates

Despite the low level of human activities, oxidation precursors have an extended lifetime in the stable atmosphere of coastal areas. Intensive photochemical reactions occur after the accumulation of precursors, resulting in local net ozone production comparable to that in the surrounding suburban environments (Zeren et al., 2022). Simultaneous observations of both urban and coastal settings in Shenzhen have indicated that the oxidation rates are comparable (Xia et al., 2021). The coupling of precursor transport and local photochemical processes in marine areas makes it meaningful to explore secondary pollution generation (Fig. 8(a), (b), and (c)). No obvious radical source was missing during the LAM and OCM periods, and the oxidation level was that expected from the base model. On a daytime basis, the mean diurnal profile of the $P(O_x)$ reached ~7 ppb/h in the LAM period, and the average nitric acid ($P(HNO_3)$) and sulfuric acid ($P(H_2SO_4)$) production rates were ~1.6 and ~0.11 ppb/h, respectively. The $P(HNO_3)$ production rate was similar to the average of observations in the Pearl River Delta region (~1.3 ppb/h), while that of the $P(H_2SO_4)$ was only half the average level (~0.24 ppb/h) (Lu et al., 2013; Tan et al., 2019b; Yang et al., 2022b). During the OCM period, the characteristics of the ocean air mass alleviated the photochemical process, and the production rates of the secondary pollutants decreased by approximately half and were close to the average levels in winter (Ma et al., 2019).

Contrary to numerous ocean observations, in the YMK site, intensive oxidation was accompanied by a high diurnal HONO level (higher than 400 ppt) (Fig. 9). The ozone levels were consistent with the Grade I air quality standard and far exceeded the global background concentration (~40 ppb). Daytime photolysis reactions of HONO contributed 1.52 ppb/h and 2.19 ppb/h to $P(RO_x)$ during the OCM and LAM periods, respectively, which were much higher than the values in several megacities during the photochemically polluted season (Tan et al., 2019a). Given the significance of HONO photolysis in driving atmospheric chemistry, a sensitivity test was

conducted without constraints on HONO (i.e., w.o HONO) to specifically quantify the contribution of HONO-induced secondary pollution. Only the homogeneous reaction (OH + NO) participated in the formation of HONO in the default mode without HONO input (Liu et al., 2022b).
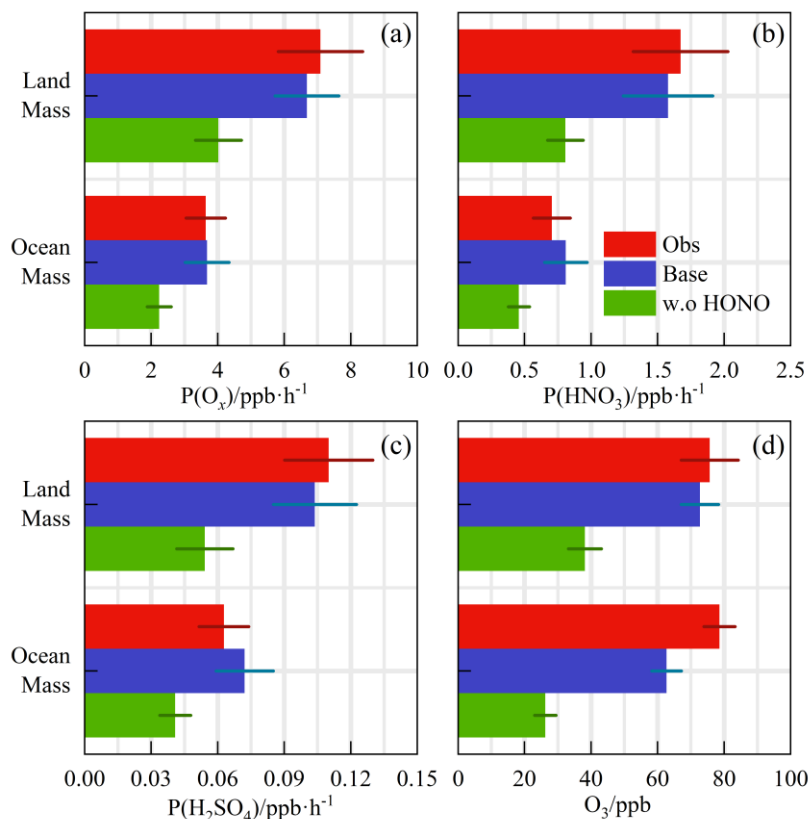
Fig. 8. The calculated reaction rates based on the observed concentrations for Land mass and Ocean mass episodes **(a)** $P(Ox)$, **(b)** $P(HNO_3)$, **(c)** $P(H_2SO_4)$. **(d)** The observed and modelled O_3 concentration with a first-order loss term. The deposition or mixing deposition processes was were equivalent to a lifetime of 15 18 hours to all species. All the rates and concentration are averaged for the daytime period between 10:00 and 15:00.

The modelled OH, HO_2 and RO_2 change when the model was unconstrained to HONO were shown in Fig. S7. After evaluation, in LAM and OCM sectors, concentration changes for OH were 46.9% and 43.2%, for HO_2 were 38.3% and 34.3%, for RO_2 were 43.7% and 39.0%, respectively. The $P(Ox)$ was found to be 33% and 39% lower during the LAM and OCM periods, respectively. The nitric acid ($P(HNO_3)$) and sulfuric acid ($P(H_2SO_4)$) formation rates also increased simultaneously (~43% and ~48% for LAM and OCM sectors, respectively). The sensitivity test identified the privileged role of the HONO-related mechanisms in the OH chemistry, which resulted in a correlation between the efficient radical recycling and secondary pollution.
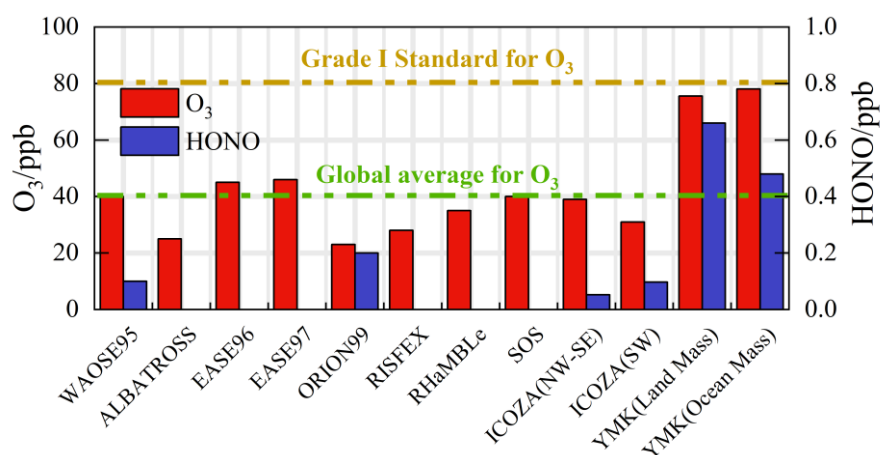
Fig. 9. Summary of both ozone and HONO concentrations in previous marine observations. The concentrations are averaged for the daytime period between 10:00 and 15:00.

A time-dependent box model was used to test the association between the HONO chemistry and the local ozone generation (Fig. 8(d)). The loss of model-generated O_3 by deposition or mixing was represented as a first-order deposition rate corresponding to a lifetime of 18 hours. ~~In order to isolate the O3 photochemical production, the impacts of vertical entrainment and horizontal advection were in general ignored.~~ Comparatively, removing the constraints on ozone and NO while keeping NO_2 as a constraint is a commonly used method in the box model for ozone prediction (Tan et al., 2018a). Considering the complexity of HONO chemistry, we emphasize that this is a sensitivity test for ozone prediction, and its validity has been examined through simulated comparisons under different HONO concentrations (Fig. S8). The observed and modelled O_3 concentrations in Fig. 8(d) are averaged for the daytime period between 10:00 and 15:00. The observed diurnal ozone concentrations were 75.7 ppb and 78.6 ppb during the LAM and OCM periods, respectively. The daytime ozone was well reproduced by the time-dependent box model, and the deviation of the simulation was less than 20% (Fig. 8(d)). After removing the HONO constraint, the simulated ozone concentrations were 38.2 and 26.3 ppb, i.e., 48% and 58% lower, during the LAM and OCM periods, respectively. Simulated O_3 decreased from ~75 ppb to a global background, and daytime HONO concentration were reduced to a low level (~70 ppt) (Woodward-Massey et al., 2022b; Zhu et al., 2022; Xia et al., 2022). The elevated daytime HONO had an additional effect on the oxidation in the background atmosphere. For coastal cities, the particularity of the HONO chemistry

in the MBL tends to influence the ozone-sensitive system and eventually magnifies the ozone background. Therefore, the promotion of oxidation by elevated precursor concentrations is worth considering when formulating emission reduction policies. In regions where HONO concentrations are elevated, the sources of HONO would need to be identified to aid pollution mitigation policies.

5 Conclusions

Comprehensive observations of HOx radicals and other relevant species were conducted in October 2019 at a coastal site in the Pearl River Delta (the YMK site, $22.55°N$, $114.60°E$). The overall air pollutants exhibited typical coastal features due to the scarce anthropogenic emissions. The daily maximum OH and HO_2 concentrations were $(4.7–9.5) \times 10^6 \, cm^{-3}$ and $(4.2–8.1) \times 10^8 \, cm^{-3}$, respectively. The base RACM2-LIM1 model satisfactorily reproduced both the observed OH and HO_2 radical concentrations, but a slight overestimation of the OH radical occurred. The daily maximum calculated total OH reactivity was $9.9 \, s^{-1}$, and nearly 70% of the reactivity was contributed by organic species.

In addition to anthropogenic and vegetation emissions, the synchronized air mass transport from the northern cities and the South China Sea exerted a time-varying influence on radical photochemistry and atmospheric oxidation. During the OCM period, the observed OH and HO_2 radical concentrations could be reflected by the base chemical mechanism, with daily average values of $4.5 \times 10^6 \, cm^{-3}$ and $4.9 \times 10^8 \, cm^{-3}$, respectively.

In the episode that was dominated by ocean mass, the $HO_2 + NO$ reaction accounted for ~50% of the primary OH yield. A higher OH generation rate was found(12.6 ppb/h) during the LAM period, and the secondary source accounted for 67% of the total, which was similar to several observations in polluted plumes. Reactions between ROx and NOx and self-combination were the main pathways of radical termination (~70%), and the contribution of peroxynitrate formation to the L(ROx) could not be ignored in the daytime.

Intensive photochemical reactions occur after the accumulation of precursors, resulting in local net ozone production comparable to that in the surrounding suburban environments. The daily average ozone production rates were 5.52 and 2.76 ppb/h in the LAM and OCM periods, respectively. The rapid oxidation process was accompanied by a higher diurnal HONO concentration (higher than 400 ppt). A non-HONO-constrained sensitivity test was performed to quantify the HONO-induced contribution to secondary pollution. After evaluation, the P(Ox) values were 33% and 39% lower during the LAM and OCM periods, respectively. The nitric acid (P(HNO$_3$)) and sulfuric acid (P(H$_2$SO$_4$)) formation rates also increased simultaneously (~43% and ~48% for LAM and OCM sectors, respectively). Simulated O$_3$ decreased from ~75 ppb to a global background, and daytime HONO concentration were reduced to a low level (~70 ppt). For coastal cities, the particularity of the HONO chemistry in the MBL tends to influence the ozone-sensitive system and eventually magnifies the ozone background. Therefore, the promotion of oxidation by elevated precursor concentrations is worth considering when formulating emission reduction policies.

Financial support

Data availability

The data used in this study are available from the corresponding author upon request (rzhu@aiofm.ac.cn).

Author contributions

27

676 WQ Liu, PH Xie, RZ Hu contributed to the conception of this study. GX Zhang and

677 RZ Hu performed the data analyses and manuscript writing. All authors contributed to

678 measurements, discussed results, and commented on the paper.

Competing interests

680 The contact author has declared that none of the authors has any competing interests.
681
682

References

Bloss, W. J., Camredon, M., Lee, J. D., Heard, D. E., Plane, J. M. C., Saiz-Lopez, A., Bauguitte, S. J. B., Salmon, R. A., and Jones, A. E.: Coupling of HOx, NOx and halogen chemistry in the antarctic boundary layer, Atmos Chem Phys, 10, 10187-10209, 10.5194/acp-10-10187-2010, 2010.

Brauers, T., Hausmann, M., Bister, A., Kraus, A., and Dorn, H.-P.: OH radicals in the boundary layer of the Atlantic Ocean: 1. Measurements by long-path laser absorption spectroscopy, Journal of Geophysical Research, 106, 7399, 10.1029/2000jd900679, 2001.

Carpenter, L. J., Fleming, Z. L., Read, K. A., Lee, J. D., Moller, S. J., Hopkins, J. R., Purvis, R. M., Lewis, A. C., Müller, K., Heinold, B., Herrmann, H., Fomba, K. W., van Pinxteren, D., Müller, C., Tegen, I., Wiedensohler, A., Müller, T., Niedermeier, N., Achterberg, E. P., Patey, M. D., Kozlova, E. A., Heimann, M., Heard, D. E., Plane, J. M. C., Mahajan, A., Oetjen, H., Ingham, T., Stone, D., Whalley, L. K., Evans, M. J., Pilling, M. J., Leigh, R. J., Monks, P. S., Karunaharan, A., Vaughan, S., Arnold, S. R., Tschritter, J., Pöhler, D., Frieß, U., Holla, R., Mendes, L. M., Lopez, H., Faria, B., Manning, A. J., and Wallace, D. W. R.: Seasonal characteristics of tropical marine boundary layer air measured at the Cape Verde Atmospheric Observatory, J Atmos Chem, 67, 87-140, 10.1007/s10874-011-9206-1, 2011.

Carslaw, N., Creasey, D. J., Heard, D. E., Lewis, A. C., McQuaid, J. B., Pilling, M. J., Monks, P. S., Bandy, B. J., and Penkett, S. A.: Modeling OH, HO2, and RO2radicals in the marine boundary layer: 1. Model construction and comparison with field measurements, Journal of Geophysical Research: Atmospheres, 104, 30241-30255, 10.1029/1999jd900783, 1999.

Chen, W., Guenther, A. B., Shao, M., Yuan, B., Jia, S., Mao, J., Yan, F., Krishnan, P., and Wang, X.: Assessment of background ozone concentrations in China and implications for using region-specific volatile organic compounds emission abatement to mitigate air pollution, Environ Pollut, 305, 119254, 10.1016/j.envpol.2022.119254, 2022.

Creasey, D. J., Heard, D. E., and Lee, J. D.: Eastern Atlantic Spring Experiment 1997 (EASE97) 1. Measurements of OH and HO2concentrations at Mace Head, Ireland, Journal of Geophysical Research: Atmospheres, 107, ACH 3-1-ACH 3-15, 10.1029/2001jd000892, 2002.

Crilley, L. R., Kramer, L. J., Pope, F. D., Reed, C., Lee, J. D., Carpenter, L. J., Hollis, L. D. J., Ball, S. M., and Bloss, W. J.: Is the ocean surface a source of nitrous acid (HONO) in the marine boundary layer?, Atmos Chem Phys, 21, 18213-18225, 10.5194/acp-21-18213-2021, 2021.

Fuchs, H., Dorn, H. P., Bachner, M., Bohn, B., Brauers, T., Gomm, S., Hofzumahaus, A., Holland, F., Nehr, S., Rohrer, F., Tillmann, R., and Wahner, A.: Comparison of OH concentration measurements by DOAS and LIF during SAPHIR chamber experiments at high OH reactivity and low NO concentration, Atmos Meas Tech, 5, 1611-1626, 10.5194/amt-5-1611-2012, 2012.

Fuchs, H., Tan, Z., Lu, K., Bohn, B., Broch, S., Brown, S. S., Dong, H., Gomm, S., Haeseler, R., He, L., Hofzumahaus, A., Holland, F., Li, X., Liu, Y., Lu, S., Min, K.-E., Rohrer, F., Shao, M., Wang, B., Wang, M., Wu, Y., Zeng, L., Zhang, Y., Wahner, A., and Zhang, Y.: OH reactivity at a rural site (Wangdu) in the North China Plain: contributions from OH reactants and experimental OH budget, Atmos Chem Phys, 17, 645-661, 10.5194/acp-17-645-2017, 2017.

Grenfell, J. L., Savage, N. H., Harrison, R. M., Penkett, S. A., Forberich, O., Comes, F. J., Clemitshaw, K. C., Burgess, R. A., Cardenas, L. M., Davison, B., and McFadyen, G. G.: Tropospheric box-modelling and analytical studies of the hydroxyl (OH) radical and related species: Comparison with observations, J Atmos Chem, 33, 183-214, 10.1023/a:1006009901180, 1999.

Griffith, S. M., Hansen, R. F., Dusanter, S., Stevens, P. S., Alaghmand, M., Bertman, S. B., Carroll, M. A., Erickson, M., Galloway, M., Grossberg, N., Hottle, J., Hou, J., Jobson, B. T., Kammrath, A., Keutsch, F. N., Lefer, B. L., Mielke, L. H., O'Brien, A., Shepson, P. B., Thurlow, M., Wallace, W., Zhang, N., and Zhou, X. L.: OH and HO_2 radical chemistry during PROPHET 2008 and CABINEX 2009-Part 1: Measurements and model comparison, Atmos Chem Phys, 13, 5403-5423, 10.5194/acp-13-5403-2013, 2013.

Huang, R. J., Hoffmann, T., Ovadnevaite, J., Laaksonen, A., Kokkola, H., Xu, W., Xu, W., Ceburnis, D., Zhang, R., Seinfeld, J. H., and O'Dowd, C.: Heterogeneous iodine-organic chemistry fast-tracks marine new particle formation, Proc Natl Acad Sci U S A, 119, e2201729119, 10.1073/pnas.2201729119, 2022.

Jiang, Y., Xue, L., Shen, H., Dong, C., Xiao, Z., and Wang, W.: Dominant Processes of HONO Derived from Multiple Field Observations in Contrasting Environments, Environmental Science & Technology Letters, 10.1021/acs.estlett.2c00004, 2022.

Kanaya, Y., Sadanaga, Y., Nakamura, K., and Akimoto, H.: Behavior of OH and HO2 radicals during the Observations at a Remote Island of Okinawa (ORION99) field campaign 1. Observation using a laser-induced fluorescence instrument, J Geophys Res-Atmos, 106, 24197-24208, 10.1029/2000jd000178, 2001.

Kanaya, Y., Yokouchi, Y., Matsumoto, J., Nakamura, K., Kato, S., Tanimoto, H., Furutani, H., Toyota, K., and Akimoto, H.: Implications of iodine chemistry for daytime HO2levels at Rishiri Island, Geophys Res Lett, 29, 45-41-45-44, 10.1029/2001gl014061, 2002.

Liu, C., Liu, G., Casazza, M., Yan, N., Xu, L., Hao, Y., Franzese, P. P., and Yang, Z.: Current Status and Potential Assessment of China's Ocean Carbon Sinks, Environ Sci Technol, 56, 6584-6595, 10.1021/acs.est.1c08106, 2022a.

Liu, P., Xue, C., Ye, C., Liu, C., Zhang, C., Wang, J., Zhang, Y., Liu, J., and Mu, Y.: The Lack of HONO Measurement May Affect the Accurate Diagnosis of Ozone Production Sensitivity, ACS Environmental Au, 10.1021/acsenvironau.2c00048, 2022b.

Liu, T., Hong, Y., Li, M., Xu, L., Chen, J., Bian, Y., Yang, C., Dan, Y., Zhang, Y., Xue, L., Zhao, M., Huang, Z., and Wang, H.: Atmospheric oxidation capacity and ozone pollution mechanism in a coastal city of southeastern China: analysis of a typical photochemical episode by an observation-based model, Atmos Chem Phys, 22, 2173-2190, 10.5194/acp-22-2173-2022, 2022c.

Lou, S., Holland, F., Rohrer, F., Lu, K., Bohn, B., Brauers, T., Chang, C. C., Fuchs, H., Haseler, R., Kita, K., Kondo, Y., Li, X., Shao, M., Zeng, L., Wahner, A., Zhang, Y., Wang, W., and Hofzumahaus, A.: Atmospheric OH reactivities in the Pearl River Delta – China in summer 2006: measurement and model results, Atmos Chem Phys, 10, 11243–11260, 10.5194/acp-10-11243-2010, 2010.

Lu, K. D., Guo, S., Tan, Z. F., Wang, H. C., Shang, D. J., Liu, Y. H., Li, X., Wu, Z. J., Hu, M., and Zhang, Y. H.: Exploring atmospheric free-radical chemistry in China: the self-cleansing capacity and the formation of secondary air pollution, Natl. Sci. Rev., 6, 579-594, 10.1093/nsr/nwy073, 2019.

Lu, K. D., Hofzumahaus, A., Holland, F., Bohn, B., Brauers, T., Fuchs, H., Hu, M., Haeseler, R., Kita, K., Kondo, Y., Li, X., Lou, S. R., Oebel, A., Shao, M., Zeng, L. M., Wahner, A., Zhu, T., Zhang, Y. H., and Rohrer, F.: Missing OH source in a suburban environment near Beijing: observed and modelled OH and HO2 concentrations in summer 2006, Atmos Chem Phys, 13, 1057-1080, 10.5194/acp-13-1057-2013, 2013.

Lu, K. D., Rohrer, F., Holland, F., Fuchs, H., Bohn, B., Brauers, T., Chang, C. C., Haeseler, R., Hu, M., Kita, K., Kondo, Y., Li, X., Lou, S. R., Nehr, S., Shao, M., Zeng, L. M., Wahner, A., Zhang, Y. H., and Hofzumahaus, A.: Observation and modelling of OH and HO_2 concentrations in the Pearl River Delta

2006: a missing OH source in a VOC rich atmosphere, Atmos Chem Phys, 12, 1541-1569, 10.5194/acp-12-1541-2012, 2012.

Ma, X. F., Tan, Z. F., Lu, K. D., Yang, X. P., Liu, Y. H., Li, S. L., Li, X., Chen, S. Y., Novelli, A., Cho, C. M., Zeng, L. M., Wahner, A., and Zhang, Y. H.: Winter photochemistry in Beijing: Observation and model simulation of OH and HO_2 radicals at an urban site, Sci Total Environ, 685, 85-95, 10.1016/j.scitotenv.2019.05.329, 2019.

Mallik, C., Tomsche, L., Bourtsoukidis, E., Crowley, J. N., Derstroff, B., Fischer, H., Hafermann, S., Hüser, I., Javed, U., Keßel, S., Lelieveld, J., Martinez, M., Meusel, H., Novelli, A., Phillips, G. J., Pozzer, A., Reiffs, A., Sander, R., Taraborrelli, D., Sauvage, C., Schuladen, J., Su, H., Williams, J., and Harder, H.: Oxidation processes in the eastern Mediterranean atmosphere: evidence from the modelling of HOx; measurements over Cyprus, Atmos Chem Phys, 18, 10825-10847, 10.5194/acp-18-10825-2018, 2018.

Niu, Y. B., Zhu, B., He, L. Y., Wang, Z., Lin, X. Y., Tang, M. X., and Huang, X. F.: Fast Nocturnal Heterogeneous Chemistry in a Coastal Background Atmosphere and Its Implications for Daytime Photochemistry, Journal of Geophysical Research: Atmospheres, 127, 10.1029/2022jd036716, 2022.

Peng, X., Wang, W. H., Xia, M., Chen, H., Ravishankara, A. R., Li, Q. Y., Saiz-Lopez, A., Liu, P. F., Zhang, F., Zhang, C. L., Xue, L. K., Wang, X. F., George, C., Wang, J. H., Mu, Y. J., Chen, J. M., and Wang, T.: An unexpected large continental source of reactive bromine and chlorine with significant impact on wintertime air quality, Natl. Sci. Rev., 8, 10.1093/nsr/nwaa304, 2021.

Qi, B., Kanaya, Y., Takami, A., Hatakeyama, S., Kato, S., Sadanaga, Y., Tanimoto, H., and Kajii, Y.: Diurnal peroxy radical chemistry at a remote coastal site over the sea of Japan, Journal of Geophysical Research, 112, 10.1029/2006jd008236, 2007.

Slater, E. J., Whalley, L. K., Woodward-Massey, R., Ye, C., Lee, J. D., Squires, F., Hopkins, J. R., Dunmore, R. E., Shaw, M., Hamilton, J. F., Lewis, A. C., Crilley, L. R., Kramer, L., Bloss, W., Vu, T., Sun, Y., Xu, W., Yue, S., Ren, L., Acton, W. J. F., Hewitt, C. N., Wang, X., Fu, P., and Heard, D. E.: Elevated levels of OH observed in haze events during wintertime in central Beijing, Atmos Chem Phys, 20, 14847-14871, 10.5194/acp-20-14847-2020, 2020.

Song, H., Lu, K., Dong, H., Tan, Z., Chen, S., Zeng, L., and Zhang, Y.: Reduced Aerosol Uptake of Hydroperoxyl Radical May Increase the Sensitivity of Ozone Production to Volatile Organic Compounds, Environmental Science & Technology Letters, 9, 22-29, 10.1021/acs.estlett.1c00893, 2021.

Stockwell, W. R., Kirchner, F., Kuhn, M., and Seefeld, S.: A new mechanism for regional atmospheric chemistry modeling, J Geophys Res-Atmos, 102, 25847-25879, 10.1029/97jd00849, 1997.

Stone, D., Whalley, L. K., and Heard, D. E.: Tropospheric OH and HO_2 radicals: field measurements and model comparisons, Chemical Society reviews, 41, 6348-6404, 10.1039/c2cs35140d, 2012.

Sun, L., Chen, T., Jiang, Y., Zhou, Y., Sheng, L., Lin, J., Li, J., Dong, C., Wang, C., Wang, X., Zhang, Q., Wang, W., and Xue, L.: Ship emission of nitrous acid (HONO) and its impacts on the marine atmospheric oxidation chemistry, Sci Total Environ, 735, 139355, 10.1016/j.scitotenv.2020.139355, 2020.

Tan, Z., Lu, K., Ma, X., Chen, S., He, L., Huang, X., Li, X., Lin, X., Tang, M., Yu, D., Wahner, A., and Zhang, Y.: Multiple Impacts of Aerosols on O(3) Production Are Largely Compensated: A Case Study Shenzhen, China, Environ Sci Technol, 10.1021/acs.est.2c06217, 2022.

Tan, Z., Lu, K., Jiang, M., Su, R., Wang, H., Lou, S., Fu, Q., Zhai, C., Tan, Q., Yue, D., Chen, D., Wang, Z., Xie, S., Zeng, L., and Zhang, Y.: Daytime atmospheric oxidation capacity in four Chinese

31

megacities during the photochemically polluted season: a case study based on box model simulation, Atmos Chem Phys, 19, 3493-3513, 10.5194/acp-19-3493-2019, 2019a.

Tan, Z. F., Lu, K. D., Jiang, M. Q., Su, R., Dong, H. B., Zeng, L. M., Xie, S. D., Tan, Q. W., and Zhang, Y. H.: Exploring ozone pollution in Chengdu, southwestern China: A case study from radical chemistry to O3-VOC-NOx sensitivity, Sci Total Environ, 636, 775-786, 10.1016/j.scitotenv.2018.04.286, 2018a.

Tan, Z. F., Lu, K. D., Dong, H. B., Hu, M., Li, X., Liu, Y. H., Lu, S. H., Shao, M., Su, R., Wang, H. C., Wu, Y. S., Wahner, A., and Zhang, Y. H.: Explicit diagnosis of the local ozone production rate and the ozone-NOx-VOC sensitivities, Sci. Bull., 63, 1067-1076, 10.1016/j.scib.2018.07.001, 2018b.

Tan, Z. F., Lu, K. D., Hofzumahaus, A., Fuchs, H., Bohn, B., Holland, F., Liu, Y. H., Rohrer, F., Shao, M., Sun, K., Wu, Y. S., Zeng, L. M., Zhang, Y. S., Zou, Q., Kiendler-Scharr, A., Wahner, A., and Zhang, Y. H.: Experimental budgets of OH, HO$_2$, and RO$_2$ radicals and implications for ozone formation in the Pearl River Delta in China 2014, Atmos Chem Phys, 19, 7129-7150, 10.5194/acp-19-7129-2019, 2019b.

Tan, Z. F., Fuchs, H., Lu, K. D., Hofzumahaus, A., Bohn, B., Broch, S., Dong, H. B., Gomm, S., Haseler, R., He, L. Y., Holland, F., Li, X., Liu, Y., Lu, S. H., Rohrer, F., Shao, M., Wang, B. L., Wang, M., Wu, Y. S., Zeng, L. M., Zhang, Y. S., Wahner, A., and Zhang, Y. H.: Radical chemistry at a rural site (Wangdu) in the North China Plain: observation and model calculations of OH, HO$_2$ and RO$_2$ radicals, Atmos Chem Phys, 17, 663-690, 10.5194/acp-17-663-2017, 2017.

Vaughan, S., Ingham, T., K.Whalley, L., Stone, D., Evans, M. J., Read, K. A., Lee, J. D., Moller, S. J., Carpenter, L. J., Lewis, A. C., Fleming, Z. L., and Heard, D. E.: Seasonal observations of OH and HO2 in the remote tropical marine boundary layer, Atmos. Chem. Phys., 12, 2149–2172, 10.5194/acp-12-2149-2012, 2012.

Wang, F., Hu, R., Xie, P., Wang, Y., Chen, H., Zhang, G., and Liu, W.: Calibration source for OH radical based on synchronous photolysis, Acta Phys Sin-Ch Ed, 69, 2020.

Wang, F. Y., Hu, R. Z., Chen, H., Xie, P. H., Wang, Y. H., Li, Z. Y., Jin, H. W., Liu, J. G., and Liu, W. Q.: Development of a field system for measurement of tropospheric OH radical using laser-induced fluorescence technique, Opt. Express, 27, A419-A435, 10.1364/oe.27.00a419, 2019.

Wang, J., Zhang, Y., Zhang, C., Wang, Y., Zhou, J., Whalley, L. K., Slater, E. J., Dyson, J. E., Xu, W., Cheng, P., Han, B., Wang, L., Yu, X., Wang, Y., Woodward-Massey, R., Lin, W., Zhao, W., Zeng, L., Ma, Z., Heard, D. E., and Ye, C.: Validating HONO as an Intermediate Tracer of the External Cycling of Reactive Nitrogen in the Background Atmosphere, Environ Sci Technol, 10.1021/acs.est.2c06731, 2023.

Wang, T., Wei, X. L., Ding, A. J., Poon, C. N., Lam, K. S., Li, Y. S., Chan, L. Y., and Anson, M.: Increasing surface ozone concentrations in the background atmosphere of Southern China, 1994-2007, Atmos Chem Phys, 9, 6217-6227, 10.5194/acp-9-6217-2009, 2009.

Wang, Y., Hu, R., Xie, P., Chen, H., Wang, F., Liu, X., Liu, J., and Liu, W.: Measurement of tropospheric HO$_2$ radical using fluorescence assay by gas expansion with low interferences, J Environ Sci (China), 99, 40-50, 10.1016/j.jes.2020.06.010, 2021.

Whalley, L. K., Furneaux, K. L., Goddard, A., Lee, J. D., Mahajan, A., Oetjen, H., Read, K. A., Kaaden, N., Carpenter, L. J., Lewis, A. C., Plane, J. M. C., Saltzman, E. S., Wiedensohler, A., and Heard, D. E.: The chemistry of OH and HO2 radicals in the boundary layer over the tropical Atlantic Ocean, Atmos Chem Phys, 10, 1555-1576, 10.5194/acp-10-1555-2010, 2010.

Woodward-Massey, R., Sommariva, R., Whalley, L. K., Cryer, D. R., Ingham, T., Bloss, W. J., Ball, S. M., Lee, J. D., Reed, C. P., Crilley, L. R., Kramer, L. J., Bandy, B. J., Forster, G. L., Reeves, C. E.,

Monks, P. S., and Heard, D. E.: Radical chemistry at a UK coastal receptor site – Part 2: experimental radical budgets and ozone production, Atmos. Chem. Phys., 10.5194/acp-2022-213, 2022a.

Woodward-Massey, R., Sommariva, R., Whalley, L. K., Cryer, D. R., Ingham, T., Bloss, W. J., Ball, S. M., Lee, J. D., Reed, C. P., Crilley, L. R., Kramer, L. J., Bandy, B. J., Forster, G. L., Reeves, C. E., Monks, P. S., and Heard, D. E.: Radical chemistry at a UK coastal receptor site – Part 1: observations of OH, HO_2, RO_2, and OH reactivity and comparison to MCM model predictions, Atmos. Chem. Phys., 10.5194/acp-2022-207, 2022b.

Xia, M., Wang, T., Wang, Z., Chen, Y., Peng, X., Huo, Y., Wang, W., Yuan, Q., Jiang, Y., Guo, H., Lau, C., Leung, K., Yu, A., and Lee, S.: Pollution-Derived Br2 Boosts Oxidation Power of the Coastal Atmosphere, Environ Sci Technol, 10.1021/acs.est.2c02434, 2022.

Xia, S.-Y., Zhu, B., Wang, S.-X., Huang, X.-F., and He, L.-Y.: Spatial distribution and source apportionment of peroxyacetyl nitrate (PAN) in a coastal region in southern China, Atmos Environ, 260, 10.1016/j.atmosenv.2021.118553, 2021.

Xu, W., Ovadnevaite, J., Fossum, K. N., Lin, C., Huang, R.-J., Ceburnis, D., and O'Dowd, C.: Sea spray as an obscured source for marine cloud nuclei, Nature Geoscience, 15, 282-286, 10.1038/s41561-022-00917-2, 2022.

Yang, X., Lu, K., Ma, X., Gao, Y., Tan, Z., Wang, H., Chen, X., Li, X., Huang, X., He, L., Tang, M., Zhu, B., Chen, S., Dong, H., Zeng, L., and Zhang, Y.: Radical chemistry in the Pearl River Delta: observations and modeling of OH and HO_2 radicals in Shenzhen in 2018, Atmos Chem Phys, 22, 12525-12542, 10.5194/acp-22-12525-2022, 2022a.

Yang, X., Lu, K., Ma, X., Gao, Y., Tan, Z., Wang, H., Chen, X., Li, X., Huang, X., He, L., Tang, M., Zhu, B., Chen, S., Dong, H., Zeng, L., and Zhang, Y.: Radical chemistry in the Pearl River Delta: observations and 2 modeling of OH and HO2 radicals in Shenzhen 2018, 10.5194/acp-2022-113, 2022b.

Yang, X., Lu, K., Ma, X., Liu, Y., Wang, H., Hu, R., Li, X., Lou, S., Chen, S., Dong, H., Wang, F., Wang, Y., Zhang, G., Li, S., Yang, S., Yang, Y., Kuang, C., Tan, Z., Chen, X., Qiu, P., Zeng, L., Xie, P., and Zhang, Y.: Observations and modeling of OH and HO_2 radicals in Chengdu, China in summer 2019, The Science of the total environment, 772, 144829-144829, 10.1016/j.scitotenv.2020.144829, 2021a.

Yang, Y., Li, X., Zu, K., Lian, C., Chen, S., Dong, H., Feng, M., Liu, H., Liu, J., Lu, K., Lu, S., Ma, X., Song, D., Wang, W., Yang, S., Yang, X., Yu, X., Zhu, Y., Zeng, L., Tan, Q., and Zhang, Y.: Elucidating the effect of HONO on O_3 pollution by a case study in southwest China, Sci Total Environ, 756, 144127, 10.1016/j.scitotenv.2020.144127, 2021b.

Zeren, Y., Zhou, B., Zheng, Y., Jiang, F., Lyu, X., Xue, L., Wang, H., Liu, X., and Guo, H.: Does Ozone Pollution Share the Same Formation Mechanisms in the Bay Areas of China?, Environ Sci Technol, 10.1021/acs.est.2c05126, 2022.

Zhang, G., Hu, R., Xie, P., Lou, S., Wang, F., Wang, Y., Qin, M., Li, X., Liu, X., Wang, Y., and Liu, W.: Observation and simulation of HOx radicals in an urban area in Shanghai, China, Sci Total Environ, 810, 152275, 10.1016/j.scitotenv.2021.152275, 2022a.

Zhang, G., Hu, R., Xie, P., Lu, K., Lou, S., Liu, X., Li, X., Wang, F., Wang, Y., Yang, X., Cai, H., Wang, Y., and Liu, W.: Intercomparison of OH radical measurement in a complex atmosphere in Chengdu, China, Sci Total Environ, 155924, 10.1016/j.scitotenv.2022.155924, 2022b.

Zhu, B., Huang, X.-F., Xia, S.-Y., Lin, L.-L., Cheng, Y., and He, L.-Y.: Biomass-burning emissions could significantly enhance the atmospheric oxidizing capacity in continental air pollution, Environ. Pollut., 285, 10.1016/j.envpol.2021.117523, 2021.

Zhu, Y., Wang, Y., Zhou, X., Elshorbany, Y. F., Ye, C., Hayden, M., and Peters, A. J.: An investigation

901   into the chemistry of HONO in the marine boundary layer at Tudor Hill Marine Atmospheric

902   Observatory in Bermuda, Atmos Chem Phys, 22, 6327-6346, 10.5194/acp-22-6327-2022, 2022.

903   Zou, Z., Chen, Q., Xia, M., Yuan, Q., Chen, Y., Wang, Y., Xiong, E., Wang, Z., and Wang, T.: OH

904   measurements in the coastal atmosphere of South China: missing OH sinks in aged air masses,

905   EGUsphere, 2022, 1-47, 10.5194/egusphere-2022-854, 2022.

906